

# Electroelastic guided wave dispersion in piezoelectric plates: Spectral methods and laser-ultrasound experiments

Cite as: J. Appl. Phys. 137, 114502 (2025); doi: 10.1063/5.0250494

Submitted: 25 November 2024 · Accepted: 23 February 2025 ·

Published Online: 20 March 2025



D. A. Kiefer,<sup>1</sup>  G. Watzl,<sup>2</sup>  K. Burgholzer,<sup>3</sup>  M. Ryzy,<sup>2</sup>  and C. Grünsteidl<sup>2,a)</sup> 

## AFFILIATIONS

<sup>1</sup>Institut Langevin, ESPCI Paris, Université PSL, CNRS, 75005 Paris, France

<sup>2</sup>Research Center for Non Destructive Testing GmbH, Altenberger Str. 69, 4040 Linz, Austria

<sup>3</sup>Institute of Semiconductor and Solid State Physics, Johannes Kepler University Linz, Altenberger Str. 69, 4040 Linz, Austria

<sup>a)</sup>Author to whom correspondence should be addressed: [clemens.gruensteidl@recendt.at](mailto:clemens.gruensteidl@recendt.at)

## ABSTRACT

Electroelastic waves in piezoelectric media are widely used in sensing and filtering applications. Despite extensive research, computing the guided wave dispersion remains challenging. This paper presents semi-analytical approaches based on spectral methods to efficiently and reliably compute dispersion curves. We systematically assess the impact of electrical boundary conditions on a 128° Y-cut LiNbO<sub>3</sub> wafer, examining open–open, open–shorted, and shorted–shorted surface configurations. Multi-modal dispersion maps obtained from laser-ultrasonic experiments for each boundary condition exhibit excellent agreement with the computational predictions. A straightforward implementation of the spectral collocation method is made available as GEW piezo plate (<https://doi.org/10.5281/zenodo.14205789>), while the spectral element method is integrated to GEWtool (<http://doi.org/10.5281/zenodo.10114243>) for multilayered plates. Therewith, we aim to make advanced semi-analytical techniques more accessible to physicists and engineers relying on dispersion analysis.

© 2025 Author(s). All article content, except where otherwise noted, is licensed under a Creative Commons Attribution-NonCommercial 4.0 International (CC BY-NC) license (<https://creativecommons.org/licenses/by-nc/4.0/>). <https://doi.org/10.1063/5.0250494>

## I. INTRODUCTION

In a waveguide, waves are constrained to travel along a defined path due to boundaries that channel the energy.<sup>1,2</sup> Guided elastic waves have applications in non-destructive testing,<sup>3</sup> material characterization,<sup>4–7</sup> and sensing.<sup>8,9</sup> If the waveguide's material is piezoelectric, the mechanical and electrical fields are coupled, resulting in electroelastic waves.<sup>1,10–13</sup> These have found widespread applications in micro-electromechanical systems (MEMS), e.g., as surface acoustic wave (SAW) devices for signal processing and sensing.<sup>14</sup> In other devices, such as bulk acoustic wave filters, spurious guided modes need to be avoided.<sup>15</sup> Due to technological advances in materials, thin film technology, and further development of MEMS devices, application-driven research on guided waves in piezoelectric plates is still very active today.<sup>16–19</sup>

Electroelastic waves in piezoelectric media are well studied. The theoretical fundamentals are covered in classic textbooks.<sup>1,2,10</sup> The initial work describes the propagation of bulk waves.<sup>12,13</sup> Work on modeling guided waves in piezoelectric plates was pioneered by

Tiersten,<sup>20</sup> who considered metallized surfaces while restricting propagation to two specific directions. Later, fundamental modes propagating along principal directions with open (unmetallized) and shorted (metallized) surfaces were studied by Joshi and Jin<sup>21</sup> and validated experimentally with interdigital transducers. Syngellakis and Lee<sup>22</sup> extended the modeling to arbitrary anisotropy and propagation direction and computed the dispersion of electrically shorted higher-order modes. Electrically open modes at different propagation directions were computed by Kuznetsova *et al.*<sup>23</sup> Sun *et al.*<sup>24</sup> presented solutions for open–open, open–shorted, and shorted–shorted surfaces. A periodic grating of open and shorted regions can be used to design phononic crystals with tunable bandgaps.<sup>25</sup> Guo *et al.*<sup>26</sup> analyzed multilayered piezoelectric plates based on a state-space formalism. Last, Zhu *et al.*<sup>27</sup> accounted for the electrical losses in the metallized surfaces of plates.

Root-searching of the characteristic equations was used in all previously mentioned studies (except the phononic crystal) to compute dispersion curves. Although this method is known to be

21 March 2025 15:29:39

slow and to miss solutions, it is still prevalent today. A software based on root-searching was made available in 1990 by Adler<sup>28</sup> and is still actively being used.<sup>29,30</sup> An alternative treatment of the transcendental characteristic equations is by analytic approximations for limiting cases.<sup>31</sup>

In contrast to root-searching of the characteristic equations, semi-analytical methods discretize the waveguide cross section and then solve a standard algebraic eigenvalue problem to reliably and efficiently obtain solutions. Various discretization methods have been used for semi-analytical models of piezoelectric waveguides. Finite elements were used very early by Lagasse<sup>32</sup> for ridge and wedge guides, while Cortes *et al.*<sup>33</sup> treated multilayered plates. Spectral methods are based on a global function basis to expand the field and are particularly well-suited for layered structures. In this context, Laguerre polynomials were used for surface waves<sup>34,35</sup> and Legendre polynomials<sup>36</sup> for plates. Laude *et al.*<sup>37</sup> used a Fourier series representation but encountered difficulties due to the non-vanishing electrical field outside the plate. Despite the advantages of semi-analytical methods, their widespread adoption is hindered by the lack of publicly available implementations and the relatively high level of knowledge on numerical computing required to implement them.

From an experimental point of view, laser-based ultrasound (LUS) has proven to be a valuable tool to precisely resolve the multi-modal dispersion curves of plates<sup>5,38–41</sup> and to access specific modes in the response spectrum.<sup>4,7,42–45</sup> Importantly, the contact-free operation of LUS allows for flexible scanning of the wave field under various environmental and boundary conditions. This is particularly valuable for model validation and for inverse characterization of material parameters. We are aware of two studies<sup>46,47</sup> that present LUS measurements of piezoelectric plates, but the effect of electrical BCs was not examined therein.

In this work, we present a semi-analytical model for guided electroelastic waves in piezoelectric plates based on spectral methods. Our focus lies on the highly instructive spectral collocation method (SCM).<sup>48–50</sup> The SCM was previously shown to be efficient and robust to compute dispersion of purely elastic waves.<sup>51,52</sup> Its main advantage is the straightforward implementation based on the underlying partial differential equations in their conventional strong form. The SCM code by Kiefer<sup>53</sup> is extended to piezoelectric plates, and we make our implementation publicly available under the name GEW piezo plate.<sup>54</sup> As an alternative, highly related method, we also introduce the spectral element method (SEM)<sup>55,56</sup> in Appendix A. While it is numerically superior to the SCM, it is at the same time conceptually more intricate. Our SEM implementation will be provided in GEWtool,<sup>57</sup> a software for guided wave analysis. Overall, we hope to demonstrate with this contribution the power of spectral methods, the simplicity of SCM, and contribute to a wider adoption of semi-analytical methods for dispersion computations. Furthermore, we validate our model with LUS experiments and contribute a compilation of multi-modal guided wave spectra in LiNbO<sub>3</sub> wafers, including two different propagation directions and three different electrical BCs.

This paper is organized in the following way: in Sec. II, we derive the guided wave problem in piezoelectric media, with focus on the treatment of electrical BCs. The implementation of the SCM is explained in Sec. III, and computational results are presented in

Sec. IV. Our LUS system is described in Sec. V. Last, measurement results are presented and discussed in Sec. VI before we conclude in Sec. VII.

## II. MODELING ELECTROELASTIC WAVES

Assuming a quasi-static electric field, we model waves in the piezoelectric medium in terms of the mechanical displacements  $\tilde{\mathbf{u}}$  and the electric potential  $\tilde{\phi}$ . The electric field intensity is  $-\nabla\tilde{\phi}$ . The piezoelectric constitutive equations relate the mechanical stress  $\tilde{\mathbf{T}}$  and electric flux density  $\tilde{\mathbf{D}}$  to  $\tilde{\mathbf{u}}$  and  $\tilde{\phi}$  by<sup>2,10,20,58</sup>

$$\tilde{\mathbf{T}} = \mathbf{c} : \nabla\tilde{\mathbf{u}} + \nabla\tilde{\phi} \cdot \mathbf{e}, \quad (1a)$$

$$\tilde{\mathbf{D}} = \mathbf{e} : \nabla\tilde{\mathbf{u}} - \boldsymbol{\epsilon} \cdot \nabla\tilde{\phi}, \quad (1b)$$

where  $\mathbf{c}$  is the fourth-order stiffness tensor at constant electric field intensity,  $\mathbf{e}$  the third order piezoelectric coupling tensor, and  $\boldsymbol{\epsilon}$  the second-order permittivity tensor at constant mechanical strain.<sup>58</sup>

For a time-harmonic field at angular frequency  $\omega = 2\pi f$ , the balance of linear momentum, i.e.,  $\nabla \cdot \tilde{\mathbf{T}} + \rho\omega^2\tilde{\mathbf{u}} = 0$ , must hold given the mass density  $\rho$ . Moreover, without free electrical charges in the material,  $\nabla \cdot \tilde{\mathbf{D}} = 0$ . On account of (1), the governing equations are<sup>1,20</sup>

$$\nabla \cdot (\mathbf{c} : \nabla\tilde{\mathbf{u}}) + \nabla \cdot (\nabla\tilde{\phi} \cdot \mathbf{e}) + \rho\omega^2\tilde{\mathbf{u}} = \mathbf{0}, \quad (2a)$$

$$\nabla \cdot (\mathbf{e} : \nabla\tilde{\mathbf{u}}) - \nabla \cdot (\boldsymbol{\epsilon} \cdot \nabla\tilde{\phi}) = 0. \quad (2b)$$

We are interested in plane waves with wavenumber  $k$  propagating in a plate of thickness  $h$  but otherwise infinite extent; see Fig. 1. The  $\mathbf{e}_x, \mathbf{e}_z$ -coordinate system (where  $\mathbf{e}_i$  with one index are the unit directional vectors) is aligned with the wave propagation such that the wave vector is along  $\mathbf{e}_x$ , while  $\mathbf{e}_z$  is the normal to the plate's surfaces. The spatiotemporal field is then of the form

$$\tilde{\mathbf{u}}(x, y, z, t) = \mathbf{u}(k, z, \omega)e^{ikx - i\omega t} \quad (3a)$$

$$\tilde{\phi}(x, y, z, t) = \phi(k, z, \omega)e^{ikx - i\omega t}, \quad (3b)$$

with  $z \in (-h/2, h/2)$ . We proceed as was done for the elastic case in Ref. 59. In account of the ansatz (3), we can use  $\nabla := ik\mathbf{e}_x + \partial_z\mathbf{e}_z$  in (2). Multiplying out, defining the second-order tensors  $\mathbf{c}_{ij} = \mathbf{e}_i \cdot \mathbf{c} \cdot \mathbf{e}_j$ , the first-order tensors  $\mathbf{e}_{ij} = \mathbf{e}_i \cdot \mathbf{e} \cdot \mathbf{e}_j$  and the scalars  $\epsilon_{ij} = \mathbf{e}_i \cdot \boldsymbol{\epsilon} \cdot \mathbf{e}_j$  and re-grouping we obtain for the<sup>60</sup>

balance of linear momentum :

$$\begin{aligned} & \left[ (ik)^2 \mathbf{c}_{xx} + ik(\mathbf{c}_{xz} + \mathbf{c}_{zx})\partial_z + \mathbf{c}_{zz}\partial_z^2 \right] \cdot \mathbf{u} + \rho\omega^2 \mathbf{u} \\ & + \left[ (ik)^2 \mathbf{e}_{xx} + ik(\mathbf{e}_{xz} + \mathbf{e}_{zx})\partial_z + \mathbf{e}_{zz}\partial_z^2 \right] \phi = \mathbf{0}, \end{aligned} \quad (4a)$$

balance of charges :

$$\begin{aligned} & \left[ (ik)^2 \epsilon_{xx} + ik(\epsilon_{xz} + \epsilon_{zx})\partial_z + \epsilon_{zz}\partial_z^2 \right] \cdot \mathbf{u} \\ & + \left[ (ik)^2 \epsilon_{xx} + ik(\epsilon_{xz} + \epsilon_{zx})\partial_z + \epsilon_{zz}\partial_z^2 \right] \phi = 0. \end{aligned} \quad (4b)$$

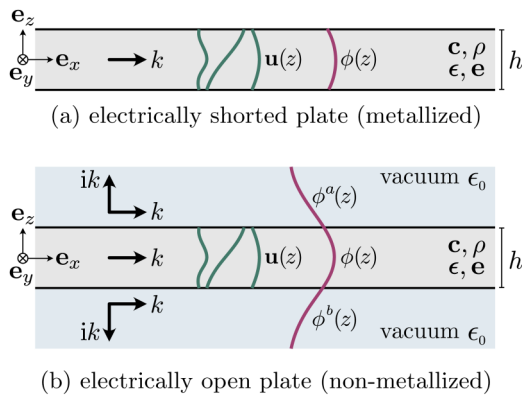


**FIG. 1.** Cross-sectional sketch of the piezoelectric plate. (a) Electrically shorted surfaces confine the field inside the plate, while (b) non-metallized surfaces lead to a nonzero electric field in the surrounding vacuum.

The above equations must hold across the thickness of the plate, i.e., for  $z \in (-h/2, h/2)$ . Note that common materials are non-gyrotropic,<sup>61</sup> meaning that their off-diagonal permittivity components  $\epsilon_{xz}$  and  $\epsilon_{zx}$  vanish. Nevertheless, we retain the corresponding term in (4b) for the sake of generality.

BCs are needed to complement (4). The plate shall be mechanically free; i.e., the tractions  $\mathbf{e}_z \cdot \mathbf{T}$  vanish at the surfaces  $z = \pm h/2$ . Using (1a) and the plane wave ansatz (3), this reads<sup>60</sup>

$$ik[\mathbf{c}_{zx} \cdot \mathbf{u} + \mathbf{e}_{zx} \phi] + \mathbf{c}_{zz} \partial_z \cdot \mathbf{u} + \mathbf{e}_{zz} \partial_z \phi = 0, \quad z = \pm h/2. \quad (5)$$

From an electrical point of view, two different kinds of BCs will be studied: (i) shorted/metallized surfaces that model an infinitely thin, perfectly conducting coating as sketched in Fig. 1(a) and (ii) the electrically open (non-metallized) surface as shown in Fig. 1(b). Any combination of these two conditions is possible at the two surfaces of the plate. If the plate is shorted at  $z = \pm h/2$ ,

$$\phi = 0 \quad \text{at } z = \pm h/2. \quad (6)$$

The open case is somewhat more intricate. Often,  $\mathbf{e}_z \cdot \tilde{\mathbf{D}} = 0$  has been used,<sup>34,35</sup> forcing the electric energy to be confined within the plate. Except for  $kh \ll 1$ , this tends to be a very good approximation because the permittivity of the piezoelectric material is usually much higher than that in vacuum.<sup>32</sup> However, the electric field in the exterior vacuum is actually nonzero, and this should be accounted for with appropriate interface conditions at the plate's surfaces. As has been shown previously,<sup>21,27</sup> this amounts to modeling inhomogeneous Neumann BCs involving the wavenumber. We pursue this approach, as the computational costs are similar and the modeling is not very complicated.

As the field is a plane harmonic wave in the plate, this must also be the case in the exterior. For  $z > h/2$ , we have  $\tilde{\phi}^a = \phi^a e^{ik_z^a(z-h/2)+ikx-iot}$ , where Snell's law has been used. In the vacuum,  $\tilde{\mathbf{D}}^a = -\epsilon_0 \nabla \tilde{\phi}^a$  and  $\nabla \cdot \tilde{\mathbf{D}}^a = 0$ , from where  $k_z^a = \pm ik$  is obtained.  $\epsilon_0$  is the permittivity of vacuum. The sign of  $k_z^a$  is chosen

such that  $\phi^a \rightarrow 0$  as  $z \rightarrow \infty$ . A similar analysis for the field below the plate shows that the opposite sign must be chosen for  $k_z^b$ . Note that the field is purely evanescent along  $z$  and carries no energy away from the plate, in accordance with the quasi-static approximation. If the plate is open at the top surface, the normal electrical flux density is required to be continuous across this interface; i.e.,  $\mathbf{e}_z \cdot \tilde{\mathbf{D}} = \mathbf{e}_z \cdot \tilde{\mathbf{D}}^{a/b}$  at  $h/2$ . Using (1b) and (3), the continuity at  $z = h/2$  reads

$$\mathbf{e}_z \cdot \mathbf{D} = [ik\mathbf{e}_{zx} + \mathbf{e}_{zz}\partial_z] \cdot \mathbf{u} - [ik\epsilon_{zx} + \epsilon_{zz}\partial_z]\phi = -i\epsilon_0 ik\phi^a, \quad (7)$$

which represents an *inhomogeneous* Neumann BC (the right-hand side is nonzero). Next, we also impose continuity of the electrical potential; i.e.,  $\phi^a = \phi(h/2)$ . Accounting for this and re-arranging in terms of  $ik$  finally yields the open-plate conditions at  $z = \pm h/2$ , namely,

$$ik[\mathbf{e}_{zx} \cdot \mathbf{u} - \epsilon_{zx}\phi \pm i\epsilon_0\phi] + \mathbf{e}_{zz}\partial_z \cdot \mathbf{u} - \epsilon_{zz}\partial_z\phi = 0, \quad (8)$$

where the positive sign is for the top surface at  $z > 0$ . Note that with  $\epsilon_0 = 0$ , this condition is identical to the commonly used approximation  $\mathbf{e}_z \cdot \tilde{\mathbf{D}} = 0$  at the surface.

### III. CALCULATION OF DISPERSION CURVES USING THE SCM

The computational method proceeds in three steps:

1. Re-write the governing equations (4) and the Neumann BCs (5) and (8) in matrix form.
2. Discretize both differential systems.
3. Incorporate the discrete BCs into the governing system. Optionally, replace the Neumann BCs with Dirichlet BCs.

In this way, an algebraic linear system is obtained that can be solved on a computer using standard techniques in order to obtain the desired guided wave solutions.

First, we collect the unknown field variables in the  $4 \times 1$ -block matrix (first block of size 3 and second block of size 1),

$$\Psi = \begin{bmatrix} \mathbf{u} \\ \phi \end{bmatrix}, \quad (9)$$

and assemble the governing equations (4a) and (4b) into one matrix equation in terms of  $\Psi$ , which yields

$$[(ik)^2 \mathcal{A} + ik(\mathcal{B} + \mathcal{B}^T)\partial_z + \mathcal{C}\partial_z^2 + \omega^2 \mathcal{M}]\Psi = 0, \quad (10)$$

with matrices

$$\mathcal{A} = \begin{bmatrix} \mathbf{c}_{xx} & \mathbf{e}_{xx} \\ \mathbf{e}_{xx}^T & -\epsilon_{xx} \end{bmatrix}, \quad \mathcal{B} = \begin{bmatrix} \mathbf{c}_{zx} & \mathbf{e}_{xz} \\ \mathbf{e}_{zx}^T & -\epsilon_{zx} \end{bmatrix}, \quad (11a)$$

$$\mathcal{C} = \begin{bmatrix} \mathbf{c}_{zz} & \mathbf{e}_{zz} \\ \mathbf{e}_{zz}^T & -\epsilon_{zz} \end{bmatrix}, \quad \mathcal{M} = \begin{bmatrix} \rho \mathbf{I} & 0 \\ 0 & 0 \end{bmatrix}. \quad (11b)$$

Therefore, we have exploited the symmetries  $\mathbf{c}_{xz} = \mathbf{c}_{zx}^T$  and  $\epsilon_{xz} = \epsilon_{zx}$  in writing the term in  $\mathcal{B} + \mathcal{B}^T$  (but note that  $\mathbf{e}_{xz} \neq \mathbf{e}_{zx}^T$  in  $\mathcal{B}$ ).

21 March 2025 15:29:39

Moreover,  $\mathbf{I}$  is the second-order identity tensor, “0” are zero-matrices of appropriate size, and all tensors are to be interpreted as the corresponding coefficient matrices. Assembling in a similar way the mechanical and electrical Neumann BCs (5) and (8) into a matrix equation gives

$$[ik(\mathcal{B} + \mathcal{V}) + C\partial_z]\Psi = 0, \quad (12)$$

where  $\mathcal{V}$  is the block matrix,

$$\mathcal{V} = \begin{bmatrix} 0 & 0 \\ 0 & \pm i\epsilon_0 \end{bmatrix}, \quad (13)$$

which accounts for the nonzero electrical flux density into the vacuum domain. The positive/negative sign is for the top/bottom boundary, respectively. For the moment, we do not need to deal with the Dirichlet BC (6) that describes shorted electrodes as it will be implemented after discretization by eliminating the corresponding degree of freedom, i.e.,  $\phi(\pm h/2)$ , which is known in advance to be zero.

Second, a large number of numerical discretization techniques could be used to obtain algebraic approximations to the boundary-value problem (10) and (12). For the numerically superior SEM, we refer to Appendix A and instead focus on the more instructive SCM in the following. The SCM is particularly simple to implement as it does not require a weak formulation nor previous meshing of the geometry. Furthermore, it exhibits exponential convergence when increasing the degrees of freedom, leading to small matrices. The Chebyshev SCM approximates an unknown function  $\phi(z)$  by a weighted superposition of the first  $N$  Chebyshev polynomials, and the error is then minimized on  $N$  so-called Chebyshev-Gauß-Lobatto collocation points  $z_i$ ,  $i \in \{1 \dots N\}$ . For details on the SCM, refer to the standard literature.<sup>48,49</sup> For implementation purposes, it is important that the method allows for the explicit construction of a differentiation matrix  $D_z$ . To explain its meaning, assume that  $\phi_d = [\phi(z_i)]$  is the mathematical vector that collects the values of  $\phi(z)$  at all collocation points  $z_i$ , and  $\phi'_d$  is the vector collecting the corresponding values of  $\partial_z \phi(z)$ . The differentiation matrix relates these two vectors through  $\phi'_d \approx D_z \phi_d$ , providing a discrete counterpart to the differentiation operation. We use the MATLAB package DMSUITE<sup>50</sup> by Weideman and Reddy to generate the differentiation matrices  $D_z$  and  $D_z^2$  of size  $N \times N$ .

The discretization of (10) is performed by formally mapping  $\partial_z \mapsto D_z$ ,  $\partial_z^2 \mapsto D_z^2$ , and for the  $\partial_z$ -independent terms  $1 \mapsto I_d$ , where  $I_d$  is the  $N \times N$ -identity matrix. Thereby, the component-wise multiplication of  $\partial_z$ ,  $\partial_z^2$ , or 1 with the matrices  $\mathcal{A}$ ,  $\mathcal{B}$ ,  $\mathcal{C}$ , or  $\mathcal{M}$  become Kronecker products,<sup>62</sup> which we denote by “ $\otimes$ .” Overall, the discrete approximation to (10) is

$$[(ik)^2 \tilde{L}_2 + ik\tilde{L}_1 + \tilde{L}_0 + \omega^2 \tilde{M}]\Psi_d = 0, \quad (14)$$

with  $4N \times 4N$  matrices,

$$\tilde{L}_2 = \mathcal{A} \otimes I_d, \quad \tilde{L}_1 = (\mathcal{B} + \mathcal{B}^T) \otimes D_z, \quad (15)$$

$$\tilde{L}_0 = \mathcal{C} \otimes D_z^2, \quad \tilde{M} = \mathcal{M} \otimes I_d. \quad (16)$$

Proceeding in the same way for the Neumann BC in (12) yields

$$[ikB_1 + B_0]\Psi_d = 0, \quad (17)$$

with

$$B_1 = (\mathcal{B} + \mathcal{V}) \otimes I_d, \quad B_0 = \mathcal{C} \otimes D_z. \quad (18)$$

Third, only the equations at  $z = \pm h/2$  are needed from (17), i.e., the equation numbers  $j \in \{1, N, N + 1, 2N, 2N + 1, 3N, 3N + 1, 4N\}$ . These BCs are incorporated into the discrete algebraic system (14) by replacing the rows  $j$  of  $\tilde{L}_i$  and  $\tilde{M}$  with the corresponding rows of  $B_i$  or zero if the term is not present in (17). The resulting matrices are denoted  $L_2$ ,  $L_1$ ,  $L_0$ , and  $M$ . In this way, we obtain the linear system

$$[(ik)^2 L_2 + ikL_1 + L_0 + \omega^2 M]\Psi_d = 0 \quad (19)$$

that fully describes plane harmonic electroelastic waves in the plate. For now, the surfaces are both electrically open as depicted in Fig. 1(b). If the plate is to be shorted at the surface corresponding to the  $i$ th collocation point  $z_i$ , we simply remove the  $3N + i$ th row and column of all matrices (the first  $3N$  corresponds to displacement degrees of freedom), thereby replacing the open condition with the Dirichlet condition given in (6).

Equation (19) represents an algebraic eigenvalue problem. By fixing  $k = k_0$ , we may compute the eigenvalues  $\omega_n^2$  with standard techniques, e.g., `eig` in MATLAB. We remark that  $M$  is a singular matrix, leading to some restrictions on the choice of the eigenvalue solver. Nonetheless, modern methods appropriately handle this case. It is also possible to do the reverse and fix the angular frequency  $\omega = \omega_0$  in order to compute the eigenvalues  $ik_n$ . This quadratic eigenvalue problem can be solved by standard companion linearization techniques as implemented in MATLAB’s `polyeig`. Note that even for real frequencies, this approach yields a *complex-valued* wavenumber spectrum;<sup>1</sup> see Appendix D. In either case, the eigenvectors  $\Psi_d$  provide access to the mechanical and electrical field distributions  $\mathbf{u}(z_i)$  and  $\phi(z_i)$ .

Our computations show very good agreement with those published by Kuznetsova *et al.*;<sup>23</sup> see Appendix B. Note that the higher the modal order (i.e., the higher the frequency), the larger the number of discretization points  $N$  needs to be. To ensure six-digit accuracy with the SCM, we use  $N = 20$  in all subsequent computations. An extended convergence analysis is presented in Appendix B. All numerical experiments are performed on one core of an Apple M1 Pro processor. Our SCM implementation uses the QZ-algorithm from MATLAB’s `eig`-function to compute a set of dispersion curves at 120  $k$ -values in 0.7 s (6 ms per  $k$ -value). The SEM implementation in GEWtool computes the same example in 0.6 s (5 ms per  $k$ -value), which is slightly faster thanks to the symmetry of the SEM matrices. However, per default GEWtool exploits subspace methods (`eigs`) and sparse matrix representation. 25 modes are located in this way in only 0.25 s (2 ms per  $k$ -value).

The presented computational method is rather easily extended to multilayered plates.<sup>52</sup> This is particularly interesting for MEMS devices, which often consist of layered structures. The layers can include piezoelectric, dielectric, and metallic media. Electrical

21 March 2025, 15:29:39

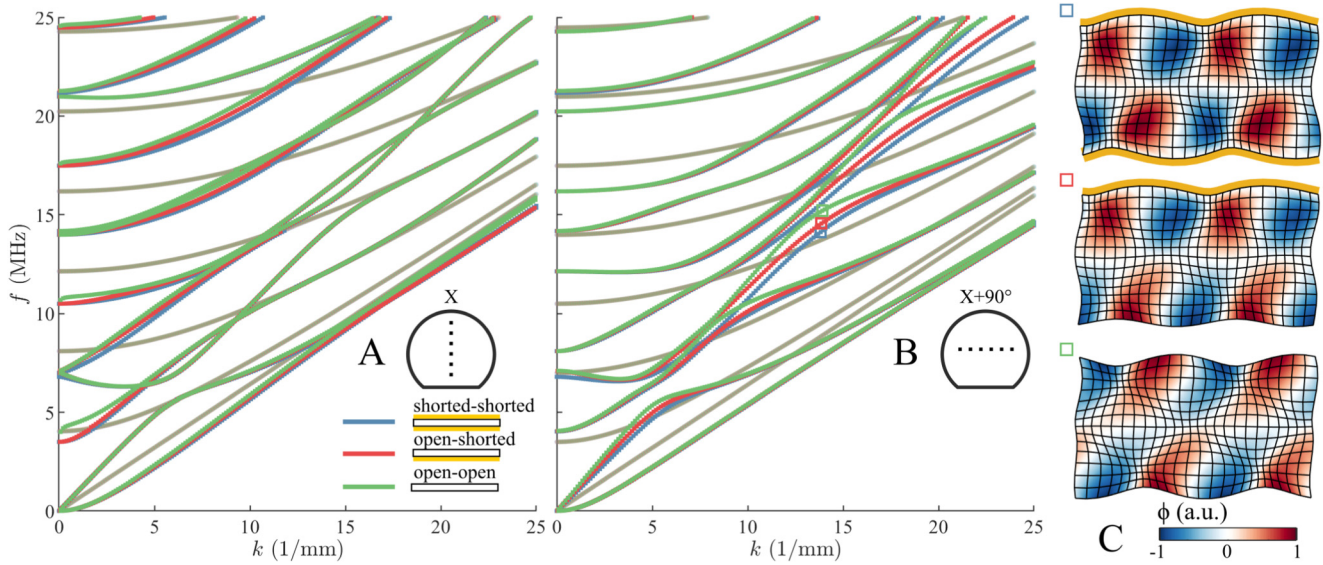


**FIG. 2.** Dispersion curves of electroelastic waves propagating in a  $128^\circ$  Y-cut  $\text{LiNbO}_3$  plate. Three different sets of electrical BCs are compared: shorted–shorted, open–shorted, and open–open. The SH-like waves are grayed-out. (a) propagation along the X axis, (b) propagation orthogonal to the X axis, and (c) displacement mode shapes (grid) and electric potential (colormap) for the points marked in (b).

currents in the latter can lead to losses, and this can be accounted for by modeling a complex effective permittivity. These extensions are concisely discussed in Appendix C for the interested reader.

#### IV. WAVES IN A $\text{LiNbO}_3$ WAFER

We now investigate guided waves in a  $510\mu\text{m}$ -thick monocrystalline  $128^\circ$  Y-cut lithium niobate ( $\text{LiNbO}_3$ ) wafer. This material is often used for MEMS as it exhibits large electromechanical coupling.<sup>61,63</sup> The material parameters are given in Appendix E. To account for the crystal orientation in the computation, we need to rotate the tensors  $\mathbf{c}$ ,  $\mathbf{e}$ , and  $\boldsymbol{\epsilon}$ —which are initially given<sup>64</sup> in the orthonormal  $\mathbf{e}_x\mathbf{e}_y\mathbf{e}_z$ -material coordinate system (Fig. 3)—to the wave propagation frame  $\mathbf{e}_x\mathbf{e}_y\mathbf{e}_z$  (Fig. 1). Here,  $\mathbf{e}_x$  lies within the wafer surface and is perpendicular to the wafer flat. The material's  $\mathbf{e}_z$  axis ( $\mathbf{e}_y$  axis) has been rotated out of the plate's normal  $\mathbf{e}_z$  by an angle of  $\mu = 38^\circ$  ( $\mu = 128^\circ$ ) around  $\mathbf{e}_x$ .

Two directions of propagation are considered: (i) along X and (ii) along  $X + 90^\circ$ , i.e., along the wafer flat; see Fig. 3. Furthermore, three different combinations of electrical BCs are systematically investigated: shorted–shorted, open–shorted, and open–open. The different BCs are compared in Fig. 2(a) for propagation along X and in Fig. 2(b) for propagation in  $X + 90^\circ$ . Several regions of the dispersion curves are observed to be quite strongly affected by the BCs, especially for propagation in  $X + 90^\circ$ . Strong electromechanical coupling can be expected in these regions. The SCM computation also provides the mechanical and electrical modal field distributions. Three examples picked at the marks in Fig. 2(b) are depicted in Fig. 2(c). Thereby, the field was extruded in the propagation direction according to the harmonic ansatz from (3).

#### V. SAMPLE PREPARATION AND LUS SYSTEM

The samples investigated were double-side polished SAW-grade  $128^\circ$  Y-cut  $\text{LiNbO}_3$  wafers with a nominal thickness of  $500\mu\text{m}$  and an average roughness specified below  $1\text{ nm}$ .<sup>65</sup> The shorted BCs were produced by depositing  $3\text{ nm}$  titanium and  $400\text{ nm}$  gold by physical vapor deposition carried out in a Balzers PLS 570, metallizing either one or both sides of the wafer.

We use a LUS system to record the spatiotemporal response of the plate. The LUS setup is sketched in Fig. 3(a). To generate

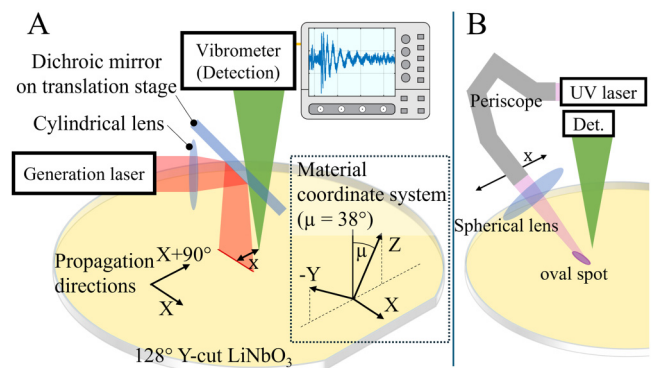


**FIG. 3.** (a) Investigated  $128^\circ$  Y-cut  $\text{LiNbO}_3$  sample and sketch of the LUS system. The orientation of the material coordinate system (X, Y, Z) and the investigated directions of propagation (X and  $X + 90^\circ$ ) are shown. (b) Workaround for uncoated sample using a UV laser at oblique incidence.

21 March 2025 15:29:39

waves, we use a pulsed laser (Bright Solutions Wedge HB 1064) with a wavelength of 1064 nm, a pulse duration of about 1.5 ns, pulse energies of approximately 2 mJ, and a pulse repetition rate set to 1000 Hz. The laser is focused by a cylindrical lens with 130 mm focal length and deflected toward the sample by  $90^\circ$  with a dichroic mirror, which is mounted on an automated translation stage. By scanning the mirror, the distance between generation and detection is varied. We deliberately moved the cylindrical lens out of the focal position by about 3 mm with the intention to couple efficiently into modes of lower  $k$  values and to avoid ablation. The cylindrical lens produces a line shaped thermo-elastic source, predominantly emitting plane waves with a wave vector perpendicular to the line.

The out-of-plane component of the resulting surface displacement  $u_z(x, t)$  is recorded with a two-wave-mixing vibrometer (Sound & Bright Tempo-FS200) operating at 532 nm wavelength connected to an oscilloscope (Teledyne LeCroy WaveRunner HRO 66Zi). The detection unit was focused onto the sample through the dichroic mirror with a lens of 100 mm focal length. A line of 14 mm was sampled along  $x$  by scanning the dichroic mirror with a pitch of  $50 \mu\text{m}$ . To improve the signal-to-noise ratio, 5000 traces were averaged for each measured position, and the bandwidth of the oscilloscope was limited to 50 MHz.

Figure 4(a) shows the recorded  $u_z(x, t)$  for the open-shorter case with propagation in the X-direction. Applying a spatiotemporal Fourier transform results in a representation of the wavefield in

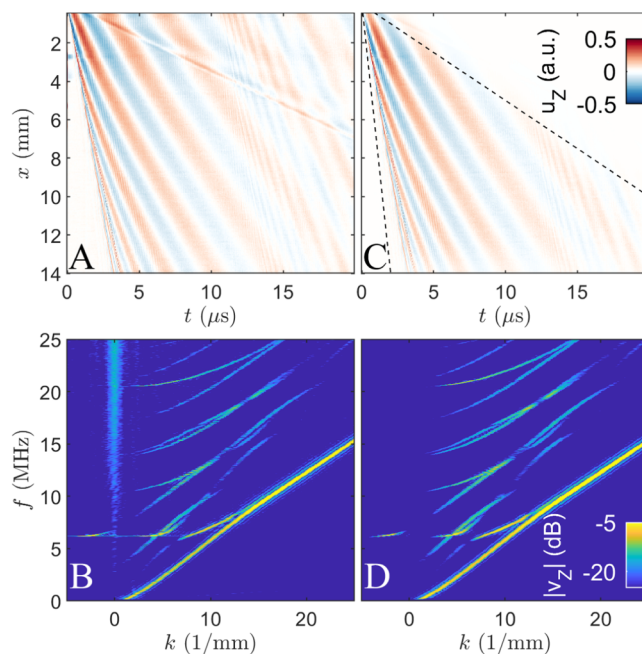


**FIG. 4.** (a) Recorded surface displacement  $u_z(x, t)$  for the open-shorter sample, propagation in the X-direction. (b) Frequency-wavenumber spectrum of (a). (c)  $u_z(x, t)$  from (a), with windowing applied. Dashed lines indicate the selected signal range. (d) Spectrum of (c), showing reduced noise and disturbances around  $k = 0$ .

the  $k$ - $f$ -domain<sup>66</sup> and is shown in Fig. 4(b), where we plot the spectral velocity magnitude  $|v_z(k, f)| = \omega |u_z(k, f)|$ .

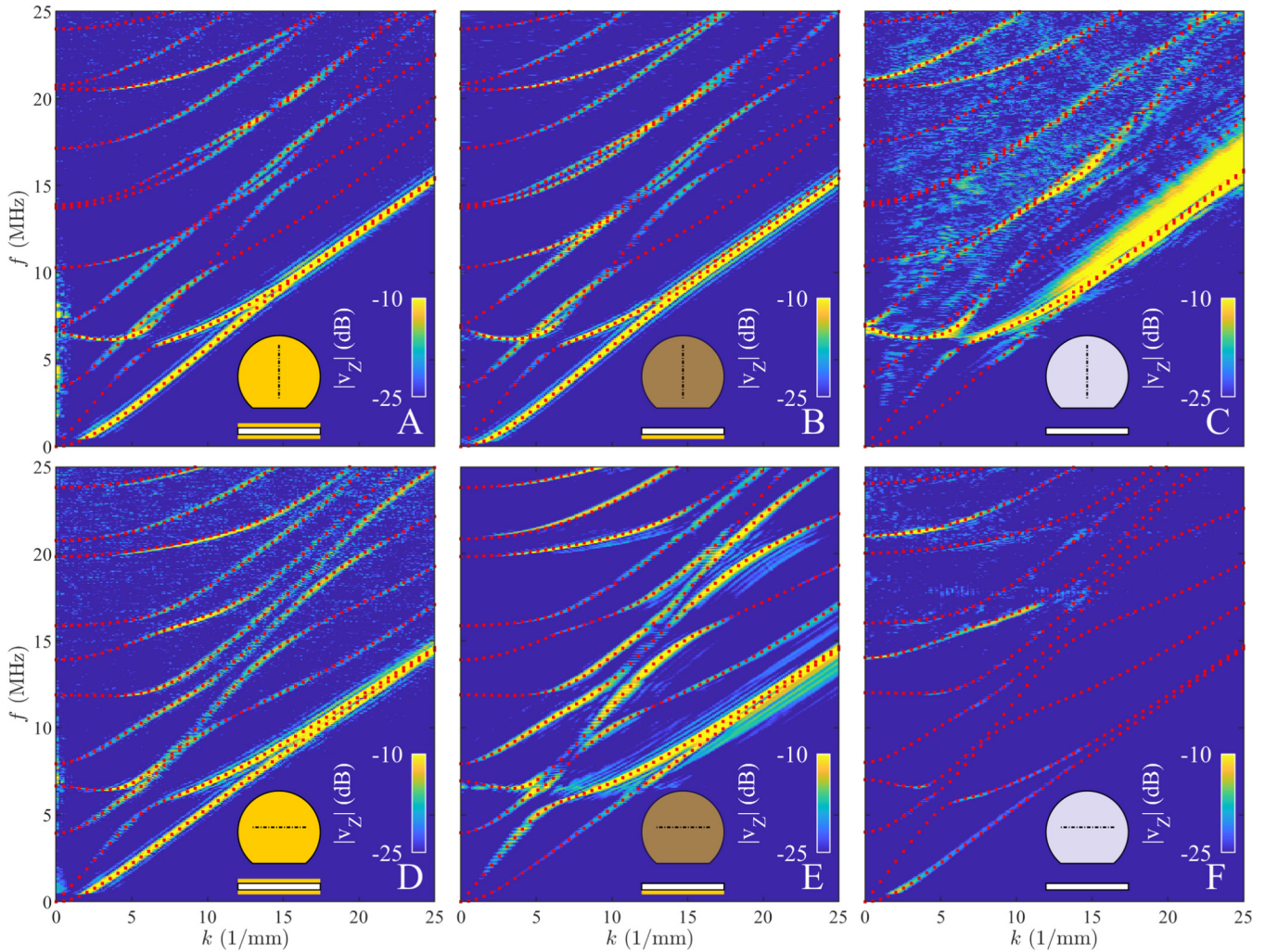
To enhance the experimental dispersion curves, we apply a window to the signals in the  $x$ - $t$ -domain. The window is designed to select contributions with energy velocities between 500 and 7000 m/s by cutting out a wedge of the data. To reduce sidelobes, the window  $w(x, t)$  is smoothed by convolution with a Hanning window in the  $x$  and  $t$  dimensions. Figure 4(c) shows the windowed signals  $u_z(x, t)w(x, t)$  and also indicates the area selected by the limiting energy velocities as dashed lines. The resulting dispersion maps with reduced noise and artifacts around  $k = 0$  are shown in Fig. 4(d). A portion of the dispersion spectrum around 6 MHz has a negative wavenumber but positive energy velocity and is, thus, detected. Such backward waves<sup>45</sup> appear in plates next to zero-group-velocity points. For simplicity, for Fig. 5, we symmetrize the measured spectra by  $v_z(k, f) + v_z(-k, f)$  and only show positive values for  $k$ .

The open-open samples are almost transparent to the 1064 nm generation laser, resulting in insufficient coupling into guided waves. We followed two separate strategies to obtain measurements in this case: First, we coated the samples with black paint, which in some attempts provided good results. Here, we reduced the generation laser energy to avoid ablation (we otherwise observed thickness resonances as the predominant contributions in the spectrum). To enhance detection on the black painted sample, we added a small dot of silver paint, which we focused the vibrometer on. Second, we used a 355 nm laser (Teem photonics PowerChip UV 355 nm) in order to exploit the significantly higher absorption of  $\text{LiNbO}_3$  in the ultraviolet (UV) spectral range. Its pulse energy was  $25 \mu\text{J}$ , the pulse length was about 1 ns, and the repetition rate was set to 250 Hz. The UV laser was guided to the sample by a flexible periscope with seven mirrors. To scan the laser along the sample, the periscope's end-piece together with a 100 mm focal length spherical lens was mounted at a linear scanning stage and pointed at the sample under an angle of  $\approx 45^\circ$ . This way, the primary setup described above could remain, while providing a workaround for the transparent sample. The workaround is shown in Fig. 3(b).

With these two strategies, we were able to produce dispersion maps of sufficient quality for comparison with the SCM. The best results are shown in Fig. 5 (UV laser in (c), black paint in (f)). We note that Yang and Tsai<sup>46</sup> successfully measured this case using a 532 nm laser and a high pulse energy of 200 mJ.

## VI. COMPARISON OF CALCULATED AND MEASURED DISPERSION CURVES

The experimental and theoretical results are superposed in Fig. 5. The computations with the SCM are shown as red dots on top of the spectral magnitude obtained by the LUS experiments. The insets indicate the direction of propagation and whether the surfaces are metallized or not. Shear-horizontal waves, which are included in the SCM result (and shown faintly in Fig. 2), are neither generated nor detected with the experimental setup and, thus, do not show. For clarity, these modes have been identified in the SCM solutions and omitted in the plot. For the calculations shown, we used measured thickness values of the samples obtained with a



21 March 2025 15:29:39

**FIG. 5.** Comparison of the LUS measurements (intensity maps) and the SCM results (points). SH-like modes are omitted from the SCM results for clarity. The BC and propagation direction are indicated by the inset sketches. (a) shorted–shorted X-direction, (b) open–shorted X-direction, (c) open–open X-direction, (d) shorted–shorted X + 90°-direction, (e) open–shorted X + 90°-direction, and (f) open–open X + 90°-direction.

micrometer screw, ranging between  $500\mu\text{m}$  and  $510\mu\text{m}$ . For the coated wafers, we used the overall thickness, including the coating.

Based on Fig. 5, excellent agreement is found between theory and experiment. Small deviations are found in the highest order modes for the coated cases. These are well explained by the finite thickness of the metallization, which is not represented in the SCM solutions here, but in an additional solution in Appendix C. Moreover, small experimental deviations from the theoretical directions of propagation cannot be excluded. We stress that the effect of different electrical BCs clearly shows in the experiment. For an assessment of the differences, refer to Fig. 2. The results obtained on the uncoated plates [Figs. 5(c) and 5(f)] exhibit a lower signal-to-noise ratio due to the workarounds described in Sec. V, but the acquired modes match well with the theory.

The configuration with the UV-laser results in an oval spot on the sample surface, rather than a line source. In this case [Fig. 5(c)], waves with arbitrary wave vector orientations are generated. All of them are potentially detected on the scan line, even when the wave vectors are not collinear to the scanning direction.<sup>67</sup> While the main features of the measured dispersion show good agreement with the calculations at fixed wave vector orientation, the blurred out regions in the experiment may be due to these wave skewing effects.

## VII. CONCLUSION

We presented the SCM to calculate dispersion curves and mode shapes for guided electroelastic waves in piezoelectric plates.

LUS experiments were conducted to measure dispersion curves on a LiNbO<sub>3</sub> wafer. Comparison of theory and experiment for different directions and electrical BCs showed excellent agreement. From these results, material characterization based on an inverse problem seems feasible. A need for new characterization techniques is especially present in the case of deposited thin films and at high frequencies. The properties of thin films often differ from the bulk material and depend on the growing process and layer thickness. We consider the possibility to measure a sample under different electrical BCs particularly promising to disentangle elastic, piezoelectric, and electric material properties.

In the context of multilayered structures, the SCM could be used in combination with LUS measurements on different production steps of a stacked MEMS device, e.g., on the pure substrate of a SAW device and then on the deposited stack, including electrodes. Previous work has proven that LUS can indeed be used to measure guided waves and resonances in the GHz range for material characterization purposes.<sup>44,68</sup> With the optical spot sizes that are achievable in practice, effective generation and detection of guided waves down to 1 μm to 2 μm wavelength is feasible.

As an alternative to SCM, we discussed the SEM in Appendix A. It is based on the weak form of the waveguide problem and is numerically superior to SCM but also somewhat more difficult to understand. An implementation of the SEM is available in GEWtool<sup>57</sup> for multilayered piezoelectric plates.

### ACKNOWLEDGMENTS

This research was funded in whole or in part by the Austrian Science Fund FWF (No. P 33764). This project is co-financed by research subsidies granted by the government of Upper Austria (No. Wi-2021-303205/13-Au). D. A. Kiefer has received support under the program “Investissements d’Avenir” launched by the French Government under Reference No. ANR-10-LABX-24. We thank Istvan Veres (Qorvo), Thomas Berer (Qorvo), and Jannis Bulling (BAM) for valuable discussions on the presented matter. For the purpose of open access, the author has applied a CC BY public copyright license to any Author Accepted Manuscript version arising from this submission.

### AUTHOR DECLARATIONS

#### Conflict of Interest

The authors have no conflicts to disclose.

#### Author Contributions

**D. A. Kiefer:** Formal analysis (lead); Funding acquisition (supporting); Methodology (equal); Software (lead); Validation (equal); Visualization (equal); Writing – original draft (equal); Writing – review & editing (equal). **G. Watzl:** Data curation (lead); Investigation (equal); Writing – review & editing (supporting). **K. Burgholzer:** Resources (lead). **M. Rzyz:** Writing – review & editing (equal). **C. Grünsteidl:** Conceptualization (lead); Formal analysis (equal); Funding acquisition (lead); Investigation (equal); Methodology (equal); Project administration (lead); Software (equal); Supervision (equal); Visualization (lead); Writing – original draft (equal); Writing – review & editing (equal).

### DATA AVAILABILITY

The data that support the findings of this study are openly available on Zenodo at <https://doi.org/10.5281/zenodo.13828765>, Ref. 69.

### APPENDIX A: SPECTRAL ELEMENT DISCRETIZATION

The spectral element method (SEM) is numerically superior to SCM because it (i) conserves the hermitian symmetry of the problem, (ii) preserves the regularity of the operators, and (iii) converges faster. These properties also facilitate the postprocessing, e.g., computation of group velocities<sup>70</sup> and zero-group-velocity points<sup>59</sup> as well as mode-sorting.<sup>71</sup> SEM is akin to the finite element method but uses high-order polynomials defined on the entire domain as a basis; i.e., no meshing is necessary. In this section, we sketch the SEM-discretization of the waveguide problem without providing theoretical details, for which we rather refer to the literature.<sup>56,72</sup>

First, the boundary-value problem (10) and (12) needs to be cast into the corresponding weak form. To this end, we introduce appropriate test functions  $\psi(z)$  corresponding to  $\Psi(z)$ , i.e., as a four-component vector function. Multiplying (10) with  $\psi^T(z)$  from the left, integrating over the domain, and performing a partial integration of the terms in  $\mathcal{B}$  and  $\mathcal{C}$  lead to the *weak form of the waveguide problem*,

$$\int_{-h/2}^{+h/2} \psi^T [(ik)^2 \mathcal{A} + ik \mathcal{B}^T \partial_z + \omega^2 \mathcal{M}] \Psi dz - \int_{-h/2}^{+h/2} \partial_z \psi^T [ik \mathcal{B} + \mathcal{C} \partial_z] \Psi dz + [\psi^T (-ik \mathcal{V}) \Psi] \Big|_{-h/2}^{+h/2} = 0. \quad (A1)$$

Thereby, we have incorporated the Neumann BC from (12) into the bracketed boundary term.

Second, discretization is performed by approximating

$$\Psi(z) \approx \sum_j \Psi_j P_j(z), \quad \psi(z) \approx \sum_i \psi_i P_i(z), \quad (A2)$$

as a weighted superposition of  $N$  known polynomials  $P_j(z)$  with  $j \in \{1 \dots N\}$  and four-component vector coefficients  $\Psi_j, \psi_i$ . We choose Lagrange polynomials  $P_j(z)$  defined on the standard Gauß–Lobatto–Legendre points.<sup>72</sup> Accounting for (A2) in (A1), the equation must hold for arbitrary  $\psi_i$  so that we can write the discrete system,

$$\left[ \underbrace{(ik)^2 \mathcal{A} \otimes PP}_{L_2} + ik \underbrace{(\mathcal{B}^T \otimes PD - \mathcal{B} \otimes PD^T - \mathcal{V} \otimes BB)}_{L_1} - \underbrace{\mathcal{C} \otimes DD}_{L_0} + \omega^2 \underbrace{\mathcal{M} \otimes PP}_{M} \right] \Psi_d = 0, \quad (A3)$$

21 March 2025 15:29:39

where  $\Psi_d = [\Psi_j]$ ,  $j \in \{1 \dots N\}$ , and the  $N \times N$ -matrices,

$$PP_{ij} := \int_{-h/2}^{+h/2} P_i P_j dz, \quad (A4a)$$

$$PD_{ij} := \int_{-h/2}^{+h/2} P_i \partial_z P_j dz, \quad (A4b)$$

$$DD_{ij} := \int_{-h/2}^{+h/2} \partial_z P_i \partial_z P_j dz, \quad (A4c)$$

$$BB_{ij} := [P_i P_j]_{-h/2}^{+h/2}. \quad (A4d)$$

Note that in (A3), we have made use of the Kronecker product between PP and  $\mathcal{A}$  (and similar for other terms), defined in block form as  $PP \otimes \mathcal{A} = [PP_{ij} \mathcal{A}]$ .  $\mathcal{A} \otimes PP$  is a permutation thereof that leads to an equally valid linear system. As usual, the matrices (A4) are computed by numerical integration of the known basis polynomials. Dirichlet BCs, e.g., electrically shorted surfaces, can be implemented by removing the corresponding degree of freedom, as was done in Sec. III. The presented SEM procedure is implemented in GEWtool<sup>57</sup> for multilayered plates. A validation and convergence analysis can be found in Appendix B.

### APPENDIX B: VERIFICATION

A comparison of phase velocity  $c_p = \omega/k$  dispersion curves calculated with the SCM (and the SEM from Appendix A) to those published by Kuznetsova *et al.*<sup>23</sup> is shown in Fig. 6 and shows very

good agreement. The latter authors employ root-finding of the characteristic equation. Two different crystal cuts of LiNbO<sub>3</sub> and propagation directions are depicted. Material constants are taken from Ref. 64 and rotated as needed before solving. Note that the root-searching method that serves as reference missed solutions, which is an inherent drawback of this method that is resolved by the semi-analytical methods proposed here.

The convergence of solutions is studied in Fig. 7 for an arbitrarily selected mode. The wavenumber is fixed at 20 rad/mm, and we compute the angular frequency  $\omega$  of the 12th mode (ordered in increasing  $\omega$ ). As reference solution  $\omega_0$ , we use a high number of discretization points of  $N = 50$ . The convergence is compared to that of the classical Finite Element Method (FEM) with first order Lagrange polynomial basis functions (implemented in this case in GEWtool using a multilayered plate). While the FEM is known to converge algebraically, spectral methods converge exponentially as long as the solution is sufficiently smooth.<sup>48,49</sup> Hence, the relative error  $|\omega - \omega_0|/\omega_0$  is seen to decrease rapidly for the spectral methods when increasing the discretization  $N$ . Particularly impressive is the rapid convergence of the SEM implemented in GEWtool (Appendix A). For this rather high-order mode, 12 accurate digits are attained already with  $N \geq 26$  for the SCM and  $N \geq 20$  for the SEM.

### APPENDIX C: METAL-PIEZOELECTRIC MULTILAYERS AND THE INFLUENCE OF THE COATINGS

It is relatively straight forward to extend both the SCM and the SEM to multilayered plates. For the SCM, the approach explained in Ref. 52 can be extended to include electrical interface conditions (continuity of  $\tilde{\phi}$  and the normal component of  $\tilde{\mathbf{D}}$ ). For the SEM, each layer is represented by one element and a

21 March 2025 15:29:39

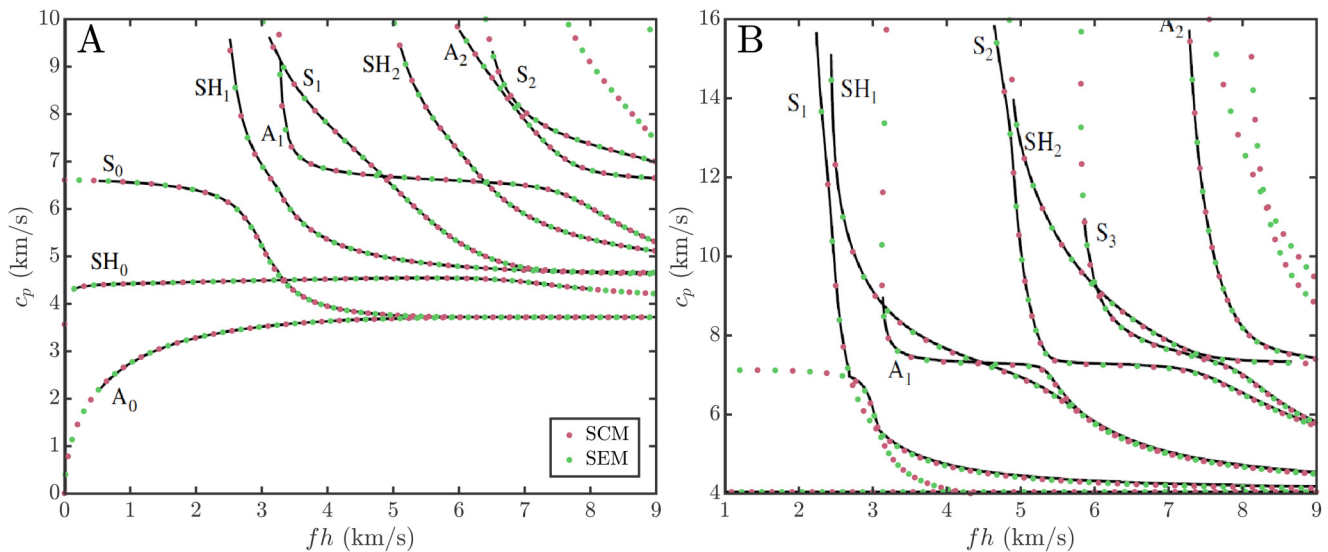
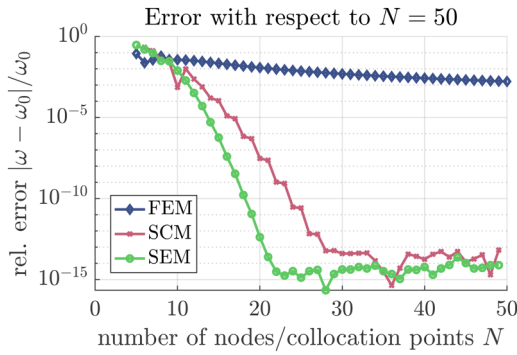


FIG. 6. Verification of the SCM and the SEM with Kuznetsova *et al.*<sup>23</sup> (black lines); (a) Y-cut, propagation in the X-direction and (b) X-cut, propagation in the  $Y + 30^\circ$ -direction.



**FIG. 7.** Convergence of the computed angular frequency  $\omega$  of the 12th mode at 20 rad/mm ( $\approx 21.7$  MHz) when increasing the number of collocation points or nodes  $N$ .

conventional element assembly is performed,<sup>72</sup> which is implemented in GEWtool.

In many situations of practical interest, piezoelectric layers are stacked between metallic and/or dielectric materials. For the latter two, the piezoelectric stress constants  $\mathbf{e}$  can be set to zero, and the effective complex electrical permittivity  $\epsilon_{\text{eff}}$  is used for  $\epsilon$ . The effective permittivity of metals is mostly imaginary due to their high electrical conductivity  $\sigma$  and is given by

$$\epsilon_{\text{eff}} = \epsilon + i \frac{\sigma}{\omega}. \quad (\text{C1})$$

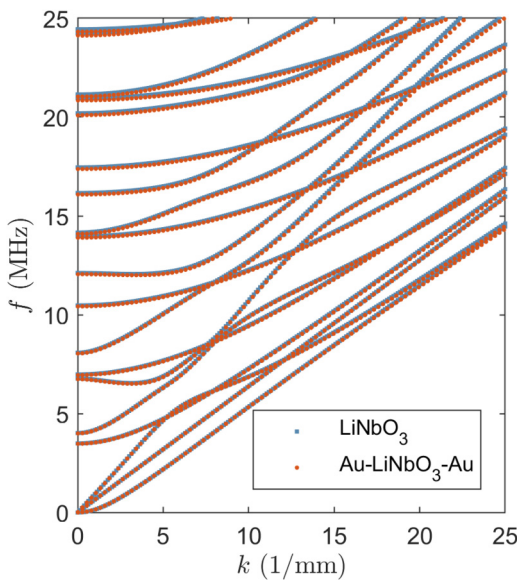


**FIG. 8.** SCM solutions for the  $X + 90^\circ$  direction in a  $128^\circ$  Y-cut LiNbO<sub>3</sub> wafer, comparing the shorted–shorted case with electrodes of zero-thickness (blue lines) to those of 400 nm thick gold (Au, red dots). The total thickness is  $500.8 \mu\text{m}$  in both cases.

A finite imaginary part accounts for losses due to electrical currents. In this case, the guided waves all have complex-valued wavenumbers and the computation needs to be performed at fixed frequencies instead of fixed wavenumbers; see Appendix D. To avoid this complication, we can model an ideal conducting layer ( $\sigma \rightarrow \infty$ , no losses). This is achieved by imposing  $\phi = 0$  over the entire layer, i.e., removing all corresponding degrees of freedom. This is equivalent to modeling pure mechanics of the layer. Yet another approach is to approximate the ideal conducting layer by fixing  $\sigma/\omega_{\text{max}} \gg \epsilon$ .

The latter approach is used in the following to assess the influence of the gold (Au) coatings. We compare solutions ignoring the gold layers ( $500.8 \mu\text{m}$  LiNbO<sub>3</sub> shorted–shorted) to those accounting for them ( $0.4 \mu\text{m}$  Au– $500 \mu\text{m}$  LiNbO<sub>3</sub>– $0.4 \mu\text{m}$  Au open–open). For gold, we use isotropic material properties ( $C_{11} = 111$  GPa,  $C_{44} = 25$  GPa,  $\rho = 19\,300$  kg/m<sup>3</sup>,  $\epsilon = 6.9\epsilon_0$  and  $\sigma = 45.2$  MS/m). Gold is an excellent conductor exhibiting  $\sigma/(\omega_{\text{max}}\epsilon) \approx 4.7 \times 10^9 \gg 1$ . Hence, the resulting wavenumbers are almost real-valued, and these solutions are shown in Fig. 8. The gold layers tend to decrease the frequency due to the effect of mass loading,<sup>1</sup> which is especially visible for the higher-order modes. This explains the small mismatch observed between LUS and SCM above 20 MHz in Fig. 5(d).

#### APPENDIX D: COMPLEX WAVENUMBER SPECTRUM

A major advantage of semi-analytical methods is the straightforward computation of the complex wavenumber spectrum. To this end, we fix real-valued frequencies in (19) and solve the quadratic eigenvalue problem in  $ik$ , which is naturally complex-valued. An example is implemented in GEW piezo plate,<sup>54</sup> and the result is reproduced in Fig. 9. The companion linearization used to solve the polynomial eigenvalue problem doubles the problem size. For this reason, the 400 frequency points in this example compute in 23 s (57 ms per  $\omega$ -point). A more efficient implementation is

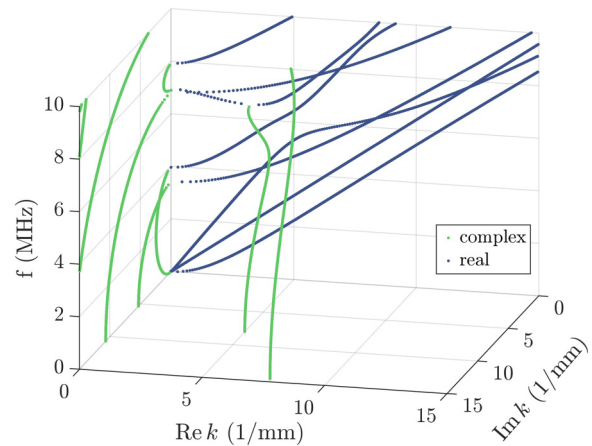


**FIG. 9.** Complex spectrum of guided waves propagating in the  $X + 90^\circ$  direction of a  $128^\circ$  Y-cut LiNbO<sub>3</sub> wafer with electrically open boundary conditions on both sides.

21 March 2025 15:29:39

provided in GEWtool's<sup>57</sup> computeK-function, which achieves the result in 4.4 s (11 ms per  $\omega$ -point). Instead of relying on MATLAB's polyeig-function, the companion linearization is solved with the subspace methods from MATLAB's eigs-function, in this case for 30 modes.

## APPENDIX E: MATERIAL PARAMETERS

The material parameters used for the LiNbO<sub>3</sub> of trigonal 3m symmetry<sup>2,61</sup> are taken from Kovacs *et al.*<sup>64</sup> We reproduce the values in Voigt-matrix notation below. Elastic stiffness under constant electric field:

$$[c] = \begin{bmatrix} 198.39 & 54.72 & 65.13 & 7.88 & 0 & 0 \\ 54.72 & 198.39 & 65.13 & -7.88 & 0 & 0 \\ 65.13 & 65.13 & 227.90 & 0 & 0 & 0 \\ 7.88 & -7.88 & 0 & 59.65 & 0 & 0 \\ 0 & 0 & 0 & 0 & 59.65 & 7.88 \\ 0 & 0 & 0 & 0 & 7.88 & 71.835 \end{bmatrix} \text{ GPa.}$$

Piezoelectric coupling tensor (piezoelectric stresses):

$$[e] = \begin{bmatrix} 0 & 0 & 0 & 0 & 3.69 & -2.42 \\ -2.42 & 2.42 & 0 & 3.69 & 0 & 0 \\ 0.30 & 0.30 & 1.77 & 0 & 0 & 0 \end{bmatrix} \text{ C/m}^2.$$

Dielectric permittivity tensor under constant strain:

$$[\epsilon] = \epsilon_0 \begin{bmatrix} 45.6 & 0 & 0 \\ 0 & 45.6 & 0 \\ 0 & 0 & 26.3 \end{bmatrix}, \quad \epsilon_0 \approx 8.854 \text{ 188 F/m.}$$

Mass density:  $\rho = 4628 \text{ kg/m}^3$ .

## REFERENCES

- B. A. Auld, *Acoustic Fields and Waves in Solids* (Wiley, New York, 1973), Vol. 2.
- D. Royer and E. Dieulesaint, *Elastic Waves in Solids I: Free and Guided Propagation* (Springer, Berlin, 1999).
- P. D. Wilcox, M. J. S. Lowe, and P. Cawley, "Mode and transducer selection for long range Lamb wave inspection," *J. Intell. Mater. Syst. Struct.* **12**, 553–565 (2001).
- D. Clorennec, C. Prada, and D. Royer, "Local and noncontact measurements of bulk acoustic wave velocities in thin isotropic plates and shells using zero group velocity Lamb modes," *J. Appl. Phys.* **101**, 034908 (2007).
- M. Thelen, N. Bochud, M. Brinker, C. Prada, and P. Huber, "Laser-excited elastic guided waves reveal the complex mechanics of nanoporous silicon," *Nat. Commun.* **12**, 3597 (2021).
- T. Grabec, Z. Soudná, K. Repčák, K. Lünser, S. Fähler, P. Stoklasová, P. Sedláč, and H. Seiner, "Guided acoustic waves in thin epitaxial films: Experiment and inverse problem solution for NiTi," *Ultrasonics* **138**, 107211 (2024).
- G. Watzl, M. Rzyz, J. A. Österreicher, A. R. Arnoldt, G. Yan, E. Scherleitner, M. Schagerl, and C. Grünsteidl, "Simultaneous laser ultrasonic measurement of sound velocities and thickness of plates using combined mode local acoustic spectroscopy," *Ultrasonics* **145**, 107453 (2025).
- F. B. Cegla, P. Cawley, and M. J. S. Lowe, "Material property measurement using the quasi-Scholte mode—A waveguide sensor," *J. Acoust. Soc. Am.* **117**, 1098–1107 (2005).
- D. A. Kiefer, A. Benkert, and S. J. Rupitsch, "Transit time of Lamb wave-based ultrasonic flow meters and the effect of temperature," *IEEE Trans. Ultrason. Ferroelectr. Freq. Control* **69**, 2975–2983 (2022).
- B. A. Auld, *Acoustic Fields and Waves in Solids* (Wiley, New York, 1973), Vol. 1.
- Z.-B. Kuang, "Electroelastic wave," in *Theory of Electroelasticity*, edited by Z.-B. Kuang (Springer, Berlin, 2014), pp. 265–337.
- J. J. Kyame, "Wave propagation in piezoelectric crystals," *J. Acoust. Soc. Am.* **21**, 159–167 (1949).
- S. Epstein, "Elastic-wave formulation for electroelastic waves in unbounded piezoelectric crystals," *Phys. Rev. B* **7**, 1636–1644 (1973).
- D. Mandal and S. Banerjee, "Surface acoustic wave (SAW) sensors: Physics, materials, and applications," *Sensors* **22**, 820 (2022).
- K. Kokkonen, T. Pensala, J. Meltaus, and M. Kaivola, "Direct measurement of spurious mode properties in thin film BAW resonator," in *Proceedings—IEEE Ultrasonics Symposium* (IEEE, 2010), pp. 420–423.
- H. Yao, P. Zheng, S. Zhang, C. Hu, X. Fang, L. Zhang, D. Ling, H. Chen, and X. Ou, "Twist piezoelectricity: Giant electromechanical coupling in magic-angle twisted bilayer LiNbO<sub>3</sub>," *Nat. Commun.* **15**, 5002 (2024).
- X. Lu and H. Ren, "Micromachined piezoelectric Lamb wave resonators: A review," *J. Micromech. Microeng.* **33**, 113001 (2023).
- F. Setiawan, M. Kadota, and S. Tanaka, "SH1 mode plate wave resonator on LiTaO<sub>3</sub> thin plate with phase velocity over 13 000 m/s," in *IEEE International Ultrasonics Symposium, IUS* (IEEE, 2021), pp. 1–4.
- C. Caliendo and M. Hamidullah, "Zero-group-velocity acoustic waveguides for high-frequency resonators," *J. Phys. D: Appl. Phys.* **50**, 474002 (2017).
- H. F. Tiersten, "Wave propagation in an infinite piezoelectric plate," *J. Acoust. Soc. Am.* **35**, 234–239 (1963).
- S. G. Joshi and Y. Jin, "Propagation of ultrasonic Lamb waves in piezoelectric plates," *J. Appl. Phys.* **70**, 4113–4120 (1991).
- S. Syngellakis and P. C. Y. Lee, "Piezoelectric wave dispersion curves for infinite anisotropic plates," *J. Appl. Phys.* **73**, 7152–7161 (1993).
- I. E. Kuznetsova, B. D. Zaitsev, I. A. Borodina, A. A. Teplyh, V. V. Shurygin, and S. G. Joshi, "Investigation of acoustic waves of higher order propagating in plates of lithium niobate," *Ultrasonics* **42**, 179–182 (2004).
- Z. Sun, Y. Mao, W. Jiang, and D. Zhang, "Influence of electrical boundary conditions on Lamb wave propagation in piezoelectric plates," in *Proceedings of the IEEE Ultrasonics Symposium* (IEEE, 1998), Vol. 1, pp. 435–438.
- C. Vasseur, C. Croënnne, J. O. Vasseur, B. Dubus, M. P. Thi, C. Prévot, and A.-C. Hladky-Hennion, "electrical evidence of the tunable electrical Bragg bandgaps in piezoelectric plates," *IEEE Trans. Ultrason. Ferroelectr. Freq. Control* **65**, 1552–1562 (2018).
- Y. Guo, W. Chen, and Y. Zhang, "Guided wave propagation in multilayered piezoelectric structures," *Sci. China Ser. G: Phys. Mech. Astron.* **52**, 1094–1104 (2009).
- F. Zhu, B. Wang, Z. Qian, I. Kuznetsova, and T. Ma, "Influence of surface conductivity on dispersion curves, mode shapes, stress, and potential for Lamb waves propagating in piezoelectric plate," *IEEE Trans. Ultrason. Ferroelectr. Freq. Control* **67**, 855–862 (2020).
- E. Adler, J. Słaboszewicz, G. Farnell, and C. Jen, "PC software for SAW propagation in anisotropic multilayers," *IEEE Trans. Ultrason. Ferroelectr. Freq. Control* **37**, 215–223 (1990).
- C. Caliendo, D. Cannatà, M. Benetti, and A. Buzzin, "UV sensors based on the propagation of the fundamental and third harmonic Rayleigh waves in ZnO/fused silica," in *2023 9th International Workshop on Advances in Sensors and Interfaces (IWASI)* (IEEE, 2023), pp. 261–266.
- N. A. Ageikin, V. I. Anisimkin, N. V. Voronova, and A. V. Smirnov, "Analysis of radiation absorption of acoustic Lamb waves in plates loaded with inviscid nonconducting liquid," *J. Commun. Technol. Electron.* **68**, 1240–1244 (2023).
- A. L. Shuvalov and E. Le Clezio, "Low-frequency dispersion of fundamental waves in anisotropic piezoelectric plates," *Int. J. Solids Struct.* **47**, 3377–3388 (2010).
- P. Lagasse, "Finite element analysis of piezoelectric elastic waveguides," *IEEE Trans. Sonics Ultrason.* **20**, 354–359 (1973).

- <sup>33</sup>D. H. Cortes, S. K. Datta, and O. M. Mukdadi, "Dispersion of elastic guided waves in piezoelectric infinite plates with inversion layers," *Int. J. Solids Struct.* **45**, 5088–5102 (2008).
- <sup>34</sup>S. Datta and B. J. Hunsinger, "Analysis of surface waves using orthogonal functions," *J. Appl. Phys.* **49**, 475–479 (1978).
- <sup>35</sup>J. E. Lefebvre, V. Zhang, J. Gazalet, and T. Gryba, "Conceptual advantages and limitations of the Laguerre polynomial approach to analyze surface acoustic waves in semi-infinite substrates and multilayered structures," *J. Appl. Phys.* **83**, 28–34 (1998).
- <sup>36</sup>X. Zhang, C. Zhang, J. Yu, and J. Luo, "Full dispersion and characteristics of complex guided waves in functionally graded piezoelectric plates," *J. Intell. Mater. Syst. Struct.* **30**, 1466–1480 (2019).
- <sup>37</sup>V. Laude, B. M. Assouar, and Z. Hou, "Computation of plate wave dispersion diagrams and surface wave velocities without explicit boundary conditions," *IEEE Trans. Ultrason. Ferroelectr. Freq. Control* **57**, 1649–1654 (2010).
- <sup>38</sup>S. G. Pierce, B. Culshaw, W. R. Philip, F. Lecuyer, and R. Farlow, "Broadband Lamb wave measurements in aluminium and carbon/glass fibre reinforced composite materials using non-contacting laser generation and detection," *Ultrasonics* **35**, 105–114 (1997).
- <sup>39</sup>F. Schöpfer, F. Binder, A. Wösthoff, T. Schuster, S. von Ende, S. Föll, and R. Lammering, "Accurate determination of dispersion curves of guided waves in plates by applying the matrix pencil method to laser vibrometer measurement data," *CEAS Aeronaut. J.* **4**, 61–68 (2013).
- <sup>40</sup>W. Rohringer, R. Sommerhuber, L. Csaszar, N. Panzer, S. Wald, B. Fischer, H. Garrecht, F. Grüner, and J. Frick, "Material characterization via contact-free detection of surface waves using an optical microphone," in *SCMT5*, edited by P. Claisse, E. Ganjian, and T. Naik (Coventry University, 2019), pp. 361–373.
- <sup>41</sup>L. Claes, H. Schmiegel, C. Grünsteidl, S. Johannesmann, M. Webersen, and B. Henning, "Untersuchung von Eigenheiten piezoelektrischer Detektionsmethoden für akustische Plattenwellen zur Materialcharakterisierung [Investigating peculiarities of piezoelectric detection methods for acoustic plate waves in material characterisation applications]," *TM. Tech. Mess.*, **88**, 147 (2021).
- <sup>42</sup>C. Prada, O. Balogun, and T. W. Murray, "Laser-based ultrasonic generation and detection of zero-group velocity Lamb waves in thin plates," *Appl. Phys. Lett.* **87**, 194109 (2005).
- <sup>43</sup>G. Watzl, C. Kerschbaummayr, M. Schagerl, T. Mitter, B. Sonderegger, and C. Grünsteidl, "In situ laser-ultrasonic monitoring of Poisson's ratio and bulk sound velocities of steel plates during thermal processes," *Acta Mater.* **235**, 118097 (2022).
- <sup>44</sup>M. Rzyz, I. Veres, T. Berer, M. Salfinger, S. Kreuzer, G. Yan, E. Scherleitner, and C. Grünsteidl, "Determining longitudinal and transverse elastic wave attenuation from zero-group-velocity Lamb waves in a pair of plates," *J. Acoust. Soc. Am.* **153**, 2090–2100 (2023).
- <sup>45</sup>D. A. Kiefer, S. Mezil, and C. Prada, "Beating resonance patterns and extreme power flux skewing in anisotropic elastic plates," *Sci. Adv.* **9**, eadk6846 (2023).
- <sup>46</sup>C. H. Yang and K. Y. Tsai, "A study on the dispersions of piezoelectric plate with laser ultrasound measurement and theoretical modeling," *Ultrasonics* **44**, 807–811 (2006).
- <sup>47</sup>G. Chen, J.-F. Zhao, and Y.-D. Pan, "Lamb wave dispersion of piezoelectric plate under laser excitation," in *2011 Symposium on Piezoelectricity, Acoustic Waves and Device Applications (SPAWDA)* (IEEE, 2011), pp. 498–501.
- <sup>48</sup>L. N. Trefethen, *Spectral Methods in MATLAB* (Society for Industrial and Applied Mathematics, Philadelphia, PA, 2000).
- <sup>49</sup>B. Fornberg, *A Practical Guide to Pseudospectral Methods*, Cambridge Monographs on Applied and Computational Mathematics (Cambridge University Press, Cambridge, 1996).
- <sup>50</sup>J. A. Weideman and S. C. Reddy, "A MATLAB differentiation matrix suite," *ACM Trans. Math. Softw.* **26**, 465–519 (2000).
- <sup>51</sup>A. T. I. Adamou and R. V. Craster, "Spectral methods for modelling guided waves in elastic media," *J. Acoust. Soc. Am.* **116**, 1524–1535 (2004).
- <sup>52</sup>F. Hernando Quintanilla, M. J. S. Lowe, and R. V. Craster, "Modeling guided elastic waves in generally anisotropic media using a spectral collocation method," *J. Acoust. Soc. Am.* **137**, 1180–1194 (2015).
- <sup>53</sup>D. A. Kiefer (2022), "GEW dispersion script." <https://doi.org/10.5281/zenodo.10641086> and [https://github.com/dakiefer/GEW\\_dispersion\\_script](https://github.com/dakiefer/GEW_dispersion_script).
- <sup>54</sup>D. A. Kiefer and C. Grünsteidl (2024), "GEW piezo plate." <https://doi.org/10.5281/zenodo.14205789> and [https://github.com/dakiefer/GEW\\_piezo\\_plate](https://github.com/dakiefer/GEW_piezo_plate).
- <sup>55</sup>A. Fichtner, *Full Seismic Waveform Modelling and Inversion*, Advances in Geophysical and Environmental Mechanics and Mathematics (Springer, Berlin, 2010).
- <sup>56</sup>H. Gravenkamp, C. Song, and J. Prager, "A numerical approach for the computation of dispersion relations for plate structures using the scaled boundary finite element method," *J. Sound Vib.* **331**, 2543–2557 (2012).
- <sup>57</sup>D. A. Kiefer (2023), "GEWtool." <https://doi.org/10.5281/zenodo.10114243> and <https://github.com/dakiefer/GEWtool>.
- <sup>58</sup>S. J. Rupitsch, *Piezoelectric Sensors and Actuators—Fundamentals and Applications*, 1st ed., Topics in Mining, Metallurgy and Materials Engineering (Springer, Berlin, 2018).
- <sup>59</sup>D. A. Kiefer, B. Plestenjak, H. Gravenkamp, and C. Prada, "Computing zero-group-velocity points in anisotropic elastic waveguides: Globally and locally convergent methods," *J. Acoust. Soc. Am.* **153**, 1386–1398 (2023).
- <sup>60</sup>Note that we exploited the symmetry  $e_{ijk} = e_{ikj}$  in the definition of  $e_{ij} := e_j \cdot (e_i \cdot e) = e_i \cdot e \cdot e_j$ .
- <sup>61</sup>R. S. Weis and T. K. Gaylord, "Lithium niobate: Summary of physical properties and crystal structure," *Appl. Phys. A* **37**, 191–203 (1985).
- <sup>62</sup>The Kronecker product  $A \otimes B$  of the  $n \times m$  matrix  $A$  and the  $p \times q$  matrix  $B$  is defined as the matrix of size  $np \times mq$  given in a block form as
- $$A \otimes B = \begin{bmatrix} A_{11}B & \cdots & A_{1m}B \\ \vdots & & \vdots \\ A_{n1}B & \cdots & A_{nm}B \end{bmatrix} ..$$
- <sup>63</sup>K. Shibayama, K. Yamanouchi, H. Sato, and T. Meguro, "Optimum cut for rotated Y-cut LiNbO<sub>3</sub> crystal used as the substrate of acoustic-surface-wave filters," *Proc. IEEE* **64**, 595–597 (1976).
- <sup>64</sup>G. Kovacs, M. Anhorn, H. E. Engan, G. Visintini, and C. C. W. Ruppel, "Improved material constants for LiNbO<sub>3</sub> and LiTaO<sub>3</sub>," in *IEEE Symposium on Ultrasonics* (IEEE, 1990), pp. 435–438.
- <sup>65</sup>UniversityWafer, Inc., <https://www.universitywafer.com>, Product ID 2559; accessed 2 February 2025.
- <sup>66</sup>D. Alleyne and P. Cawley, "A two-dimensional fourier transform method for the measurement of propagating multimode signals," *J. Acoust. Soc. Am.* **89**, 1159–1168 (1991).
- <sup>67</sup>D. A. Kiefer, S. Mezil, and C. Prada, "Extreme wave skewing and dispersion spectra of anisotropic elastic plates," *Phys. Rev. Res.* **7**(1), L012043 (2025).
- <sup>68</sup>C. Grünsteidl, I. Veres, T. Berer, S. Kreuzer, R. Rothemund, M. Hettich, E. Scherleitner, and M. Rzyz, "Measurement of the attenuation of elastic waves at GHz frequencies using resonant thickness modes," *Appl. Phys. Lett.* **117**, 164102 (2020).
- <sup>69</sup>D. A. Kiefer, G. Watzl, K. Burgholzer, M. Rzyz, and C. Grünsteidl, "Electroelastic guided wave dispersion in piezoelectric plates: Spectral methods and laser-ultrasound experiments," Dataset, Zenodo, CERN, 2024. <https://doi.org/10.5281/zenodo.13828765>.
- <sup>70</sup>S. Finnveden, "Evaluation of modal density and group velocity by a finite element method," *J. Sound Vib.* **273**, 51–75 (2004).
- <sup>71</sup>H. Gravenkamp, B. Plestenjak, and D. A. Kiefer, "Notes on oscillations and mode tracing in semi-analytical waveguide modeling," *Ultrasonics* **135**, 107112 (2023).
- <sup>72</sup>T. J. R. Hughes, *The Finite Element Method: Linear Static and Dynamic Finite Element Analysis* (Dover Publications, Mineola, NY, 2012).